Environmental Science Processes & Impacts

ROYAL SOCIETY OF CHEMISTRY

PAPER

View Article Online
View Journal | View Issue

Check for updates

Cite this: *Environ. Sci.: Processes Impacts*, 2026, **28**, 998

$PM_{2.5}$ nitrate formation during winter haze episodes: insights from Seoul, South Korea

Hyunmin Lee, [a] Meehye Lee,*[a] Saehee Lim,*[bc] Lim-Seok Chang,[d] Kyunghwan Kim,[e] Yuri Choi,[f] Moon-Soo Park,[g] Junsu Gil, [ah] Joo-Ae Kim[ah] and Changdong Yun[a]

This study investigates the formation and accumulation mechanisms of particulate nitrate (NO_3^-) during haze events in early winter 2021 in Seoul, South Korea, based on intensive ground-based observations from the Satellite Integrated Joint Monitoring of Air Quality (SIJAQ) campaign. Hourly measurements of particulate matter (PM), major $PM_{2.5}$ components and precursor gases revealed a strong correlation between $PM_{2.5}$ mass and NO_3^-, particularly during high-pollution episodes, with synoptic meteorological conditions exerting a dominant influence on NO_3^- variability. Under anticyclonic conditions, nocturnal gas-to-particle conversion and limited vertical mixing facilitated NO_3^- accumulation, followed by daytime volatilization at elevated temperatures and enhanced aerosol acidity. In contrast, cold frontal passages promoted rapid and sustained NO_3^- enhancement through regional transport and vertical entrainment, with elevated concentrations persisting during the subsequent stagnation of the air mass. Thermodynamic analysis indicated that ammonium nitrate formation was favored in both regimes, with ambient precursor levels frequently exceeding equilibrium thresholds. NO_3^- enrichment coincided with the increase in droplet-mode particles providing volume for secondary formation. Planetary boundary layer height (PBLH) variations further modulated surface concentrations by influencing vertical mixing and dilution. These findings highlight the complex interplay among local chemistry, aerosol microphysics and synoptic meteorology in driving wintertime haze formation in East Asian megacities, with implications for forecasting and mitigation strategies.

Received 30th July 2025
Accepted 13th February 2026

DOI: 10.1039/d5em00589b

rsc.li/espi

Environmental significance

Fine particulate matter ($PM_{2.5}$) pollution during winter haze events in East Asian megacities presents serious environmental and health concerns. Understanding the formation of particulate nitrate (NO_3^-), a major $PM_{2.5}$ component, is essential for effective control strategies. This study reveals that NO_3^- accumulation in Seoul is driven by nocturnal chemistry in stagnant anticyclones and enhanced by regional transport during frontal passages. It also shows that surface concentrations are strongly influenced by boundary layer dynamics and the behavior of aerosol particles. These findings underscore the need to integrate meteorological conditions and aerosol processes into air quality management frameworks to mitigate wintertime haze pollution.

1 Introduction

High concentrations of particulate matter (PM) have become a significant global public health concern due to its association with premature mortality. Consequently, many countries have reinforced air quality policies to manage these pollutants.[1,2] For instance, in Europe, one of the most urbanized regions worldwide, $PM_{2.5}$ concentrations decreased from 2003 to 2019 due to effective policy controls for air pollution.[3] East Asia experiences particularly high $PM_{2.5}$ concentrations, driven by rapid industrialization and urbanization. Specifically, in China, sulfur dioxide (SO_2) emissions from fossil fuel combustion have been stringently regulated over the past two decades;[4,5] this has led to a decrease in $PM_{2.5}$ concentrations, with 53% of the country's cities reporting annual average concentrations below 35 $\mu g\ m^{-3}$. However, high-$PM_{2.5}$ concentrations persist in many regions, particularly nitrate levels, during winter.[6,7]

In South Korea, $PM_{2.5}$ has been designated as a criteria air pollutant and has been officially measured since 2015. $PM_{2.5}$ concentrations in Seoul are generally higher during the cold season between December and March.[8] To address this, a seasonal control system has been implemented during winter

[a]Department of Earth and Environmental Sciences, Korea University, Seoul, South Korea. E-mail: meehye@korea.ac.kr
[b]Department of Environmental Engineering, Chungnam National University, Daejeon, South Korea. E-mail: saehee.lim@cnu.ac.kr
[c]Department of Environmental and IT Convergence, Chungnam National University, Daejeon, South Korea
[d]Environmental Satellite Center, National Institute of Environmental Research, Incheon, South Korea
[e]Climate and Environmental Research Institute, Korea Institute of Science and Technology, Seoul, South Korea
[f]Living Environment Research Division, Seoul Metropolitan Government Research Institute of Public Health and Environment, Seoul, South Korea
[g]Department of Climate and Environment, Sejong University, Seoul, South Korea
[h]The Institute of Basic Science, Korea University, Seoul, South Korea

since 2019.[9] During the COVID-19 pandemic in 2020, annual average $PM_{2.5}$ concentrations decreased in Seoul, particularly in winter, due to a significant reduction in emissions. However, despite lower annual average $PM_{2.5}$ concentrations due to policy controls, frequent and elevated concentrations of $PM_{2.5}$ were observed in the city in early winter 2021, especially in November, with a high proportion of particulate nitrate (NO_3^-).[10]

Therefore, despite the regulation of $PM_{2.5}$ precursor gases, high-$PM_{2.5}$ concentrations persist in East Asia. These cannot be significantly mitigated by conventional emission controls alone, primarily because $PM_{2.5}$ is mainly formed through secondary reactions. Given the ongoing urbanization in the region,[11] high-$PM_{2.5}$ events are expected to continue. Therefore, it is important to analyze high-NO_3^- events that drive this phenomenon.

Nitric acid (HNO_3), a precursor to NO_3^-, is produced by the reaction between nitrogen oxides ($NO_x \equiv NO + NO_2$) and hydroxyl radicals (OH) during the day or by heterogeneous reactions through ozone (O_3) oxidation at night, as summarized below:[12]

$$NO_2(g) + OH(g) \rightarrow HNO_3(g) \quad (R1)$$

$$2NO_2(g) + H_2O(g) \rightarrow HONO(g) + HNO_3(g) \quad (R2)$$

$$HNO_3(g) + NH_3(g) \xrightarrow{K_{sp},\ DRH} NH_4^+(aq) + NO_3^-(aq) \quad (R3)$$

$$NO_2(g) + O_3(g) \rightarrow NO_3(g) + O_2(g) \quad (R4)$$

$$NO_3(g) + NO_2(g) \leftrightarrow N_2O_5(g) \quad (R5)$$

$$N_2O_5(g) + H_2O(l) \rightarrow 2H^+(aq) + 2NO_3^-(aq) \quad (R6)$$

where K_{sp} represents a solid product and DRH is the deliquescence relative humidity. The resulting HNO_3 reacts with the alkaline precursor gas ammonia (NH_3) to form ammonium nitrate (NH_4NO_3), which is then converted to NO_3^-. These reactions typically occur when the precursor gases reach thermodynamic equilibrium (which is influenced by temperature and humidity), leading to the formation of secondary inorganic aerosols that are ultimately removed as ions.[13,14] To understand NO_3^- formation mechanisms, it is essential to determine the distribution of precursor gases such as HNO_3 and NH_3 through detailed measurements. However, these gases are highly soluble in water and highly reactive on surfaces, complicating ground-level measurements due to interference. In Seoul, $PM_{2.5}$ composition is measured hourly using an ambient ion monitor (AIM) connected to a $PM_{2.5}$ cyclone (URG-9000D), which is employed as the Korean standard method for such measurements.[10] In addition, an aerosol mass spectrometer (AMS) typically quantifies the organic and inorganic composition of PM_1.[15] However, these measurements usually target PM_1 and are not directly comparable to other real-time data. During airborne observations, HNO_3 is mainly measured using a chemical ionization mass spectrometer (CIMS).[16] However, on the ground, it is commonly treated as total nitrate ($tNO_3 \equiv NO_3^- + HNO_3$), with such measurements being relatively scarce. Meanwhile, NH_3 has been measured using ion chromatography (IC)-based analytical methods with a high-efficiency diffusion scrubber, or more recently using cavity ring-down spectroscopy (CRDS).[17]

Recent advancements in denuder systems that capture precursor gases (*e.g.*, miniaturization) have simplified their use and lowered detection limits, permitting the simultaneous analysis of secondary inorganic aerosols and precursor gases to $PM_{2.5}$ using devices such as AIMs or Monitor for AeRosols and Gases in ambient Air (MARGA) systems. Using a MARGA, measurement errors can be reduced by injecting lithium bromide (LiBr) internal standards to verify concentrations in real-time, allowing more accurate analysis of particle–gas interactions. Owing to the advantages of the MARGA system, it has been widely used by researchers.[18,19] In particular, China has established a national measurement network that utilizes the MARGA system for long-term monitoring and scientific research.[20–23]

To determine the formation mechanisms of high early-winter NO_3^- levels in South Korea, in October and November 2021, Satellite Integrated Joint Monitoring of Air Quality (SIJAQ) was conducted in Seoul, with Olympic Park as the primary measurement site, as a preliminary campaign for the Airborne and Satellite Investigation of Asian Air Quality (ASIA-AQ) mission, which was conducted in winter 2024. As a part of SIJAQ, the present study was conducted in central Seoul during the same period, observing high-$PM_{2.5}$ events.[24] This enabled the physical and chemical atmospheric properties to be analyzed to identify the key factors influencing the occurrence of high-NO_3^- concentrations during the cold season. The results of this study provide a basis for understanding the causes of high-NO_3^- concentrations in East Asian megacities and developing effective air quality management strategies.

2 Methods

The major $PM_{2.5}$ components (NO_3^-, SO_4^{2-} and NH_4^+) and their precursor gases (HONO, HNO_3 and NH_3) were measured at 1 h intervals using a MARGA (2060 MARGA R, Metrohm AG, Herisau, Switzerland). Additionally, organic carbon (OC) and elemental carbon (EC) were measured at 1 h intervals using a semi-continuous OC-EC field analyzer (Model 4, Sunset Laboratory, Inc., Tigard, OR, USA). All measurements were performed on the seventh floor of the Mediheal EES Hall at Korea University in Seoul between 18 October and 25 November 2021. Korea University is located northeast of central Seoul, with a highway and commercial complexes located within 1 km (Fig. S1).

2.1 Measurement of major $PM_{2.5}$ components

The MARGA drew air through an impactor at a flow rate of 16.7 L min^{-1}. The sampled air passed through a wet rotating denuder, where the gas-phase components were primarily captured in the liquid phase. The denuder showed a capture efficiency of over 99%. The detection limits were as follows (in units of μg m^{-3} unless otherwise specified): Cl^-: 0.01, NO_3^-:

0.03, SO_4^{2-}: 0.02, Na^+: 0.04, NH_4^+: 0.04, K^+: 0.08, Mg^{2+}: 0.02, Ca^{2+}: 0.04, HONO: 0.02, HNO_3: 0.03 and NH_3: 0.03. The gas- and particulate-phase concentrations of the analyzed species were calculated in real-time based on the concentration and theoretical conductivity of the mixed LiBr solution in the liquid sample injected into the IC system and were then calculated as the gas-phase concentration.

QA/QC included an hourly LiBr internal standard introduced into both the gas and particle channels to track sample-volume-related uncertainty and to normalize ion responses. Ion chromatography performance was verified with weekly multielement external standards (linearity and retention-time checks). Over the campaign, the particle-phase ion balance (in equivalents) was 1.01 ± 0.10, and total ammonia ($t\mathrm{NH_3} \equiv \mathrm{NH_4^+} + \mathrm{NH_3}$) correlated strongly ($r = 0.91$) with $t\mathrm{NO_3}$ supporting internally consistent and reliable MARGA measurements.

2.2 Organic carbon and elemental carbon

The semi-continuous OC-EC field analyzer drew air through the impactor at a flow rate of 8 L min^{-1}. The concentrations of OC and EC were measured in real-time by burning samples collected on quartz filters at 1 h intervals and measuring the resulting carbon dioxide (CO_2). The analysis protocol was adapted from NIOSH 5040 methods. Thermal-optical transmittance was used to measure CO_2. During the analysis, helium (99.999%), a mixture of helium and methane (5%) and a mixture of helium and oxygen (10%) were injected for analysis. The detection limits for OC and EC were 0.2 and 0.1 μg m^{-3}, respectively.

2.3 Reactive gases, particle numbers and meteorological variables

$PM_{2.5}$, PM_{10}, O_3 and NO_2 were measured at the nearest Air Pollution Monitoring Network station (Dongdaemun-gu site). The size distribution and number concentration of the aerosol particles were obtained with a scanning mobility particle sizer (SMPS) and aerodynamic particle sizer (APS) at Olympic Park and the National Institute of Environmental Research (NIER) Seoul supersite, respectively.[24] The hourly concentration of total volatile organic compounds (TVOCs) was determined every hour at the Jongno-gu site of the Seoul Metropolitan Government Research Institute of Public Health and Environment (SIHE) network, located in central Seoul.[25] Meteorological variables were obtained from the Seoul reference site run by the Korea Meteorological Administration (KMA). The locations of the measurement sites are presented in Fig. S1.

2.4 Planetary boundary layer height

During the SIJAQ campaign, the planetary boundary layer height (PBLH) was estimated using measurements from a lidar-type ceilometer (CL51, Vaisala Oyj, Vantaa, Finland) near Korea University in Seoul (Fig. S1). The CL51 measures the strength of the emitted light signal that is backscattered by atmospheric aerosols. The PBLH was estimated by combining the backscattering coefficient and the Integrated System for Atmospheric Boundary Layer Height Estimation (ISABLE) algorithm.[26] The ISABLE algorithm determines an optimal PBLH by post-processing the outputs of *k*-means clustering and density-based spatial clustering of applications with noise (DBSCAN). This post-processing is performed among a maximum of 19 PBLH candidates that were initially calculated using conventional techniques, including time-variance, gradient, wavelet and clustering.[27–30]

2.5 Estimation of aerosol liquid water content and pH using the ISORROPIA II model

The ISORROPIA II thermodynamic model was used to calculate the aerosol liquid water content (ALWC) and pH of aerosols. This model computes the equilibrium state of a mixed system consisting of Cl^-, NO_3^-, SO_4^{2-}, Na^+, NH_4^+, K^+, Mg^{2+}, Ca^{2+} and H_2O at a given temperature and relative humidity.[31] To enhance the computation speed, ISORROPIA II assumes bulk properties and considers dissolved components to be in equilibrium with the gas phase without phase separation. This model operates based on a forward-problem approach, starting from initial conditions and progressing toward equilibrium. In this study, the forward method was employed, and the phase state was considered metastable, allowing the model to retain stability over a certain period despite being energetically unstable with environmental changes.

2.6 Calculation of air-mass trajectories using the HYSPLIT model

In this study, the Hybrid Single-Particle Lagrangian Integrated Trajectory (HYSPLIT) model was used to track the transport path of atmospheric particles. HYSPLIT was developed by the National Oceanic and Atmospheric Administration (NOAA) and is widely used to calculate the trajectory of air masses. The meteorological data used for the trajectory analysis were sourced from the Global Data Assimilation System (GDAS), which integrates observational data collected globally to provide a comprehensive analysis of atmospheric conditions. These data enable the model to more accurately reproduce various chemical and physical atmospheric processes. A 48 h backward trajectory analysis was conducted, with particle release altitudes set to 500 m. The model was run at different altitudes to examine the vertical structures affecting stagnant conditions.

3 Results and discussion

3.1 Measurement overview in urban Seoul during the SIJAQ campaign

During the experiment, $PM_{2.5}$ mass concentrations varied widely, ranging from 1 to 140 μg m^{-3} (Fig. S2). The average concentrations of $PM_{2.5}$, PM_{10}, major $PM_{2.5}$ components and precursor gases were as follows (in units of μg m^{-3} unless otherwise specified): $PM_{2.5}$: 25, PM_{10}: 41, NO_3^-: 7.83, SO_4^{2-}: 2.92, NH_4^+: 3.23, OC: 3.70, EC: 1.26, HNO_3: 0.13 ppbv and NH_3: 6.52 ppbv (Table 1). Among the constituents of $PM_{2.5}$, the concentration of the secondary inorganic species NO_3^- increased significantly with increasing $PM_{2.5}$ levels. PM_{10}

concentrations also increased alongside $PM_{2.5}$, resulting in higher $PM_{2.5}/PM_{10}$ ratios during high-$PM_{2.5}$ events. The precursor gases NO_2 and VOCs exhibited typical diurnal variations, peaking in the early morning and late morning, respectively, and the concentrations of both varied dynamically with $PM_{2.5}$ levels (Fig. S4). In contrast, NH_3 remained relatively stable, with levels lower than the annual average throughout the experiment, showing only a slight increase with $PM_{2.5}$. Although HNO_3 mixing ratios stayed below ppb levels for most of the experiment, a nighttime increase was observed in early November.

High-$PM_{2.5}$ concentrations were observed episodically, with levels exceeding the 24 h average of 25 μg m^{-3} specified in the World Health Organization's 2005 air quality guidelines. Four high-$PM_{2.5}$ events were recorded: 26 and 27 October (Case 1), 3–6 November (Case 2), 14–16 November (Case 3) and 18–21 November (Case 4). The measured chemical and meteorological characteristics during these cases are summarized in Table 1.

Table 1 Mean values (and ranges for the entire campaign) of meteorological variables, $PM_{2.5}$, PM_{10}, $PM_{2.5}$ components and precursor gas concentrations for the four high-$PM_{2.5}$ events during the experimental period

Species (unit)	Average (range)	Case 1	Case 2	Case 3	Case 4
T^a (°C)	9.9 (−3.5–21.1)	13.2	12.8	10.0	11.4
WS^a (m s^{-1})	2.0 (0.0–6.8)	1.9	1.5	1.9	2.0
RH^a (%)	67 (29–96)	69	70	69	77
$PBLH^a$ (m)	816 (137–2384)	658	642	785	575
$PM_{2.5}$ (μg m^{-3})	25 (1–140)	30	36	30	76
PM_{10} (μg m^{-3})	41 (3–182)	47	53	54	104
NO_3^- (μg m^{-3})	7.83 (0.08–52.48)	10.46	10.28	9.06	28.74
SO_4^{2-} (μg m^{-3})	2.92 (0.27–13.37)	2.87	4.82	2.11	8.12
NH_4^+ (μg m^{-3})	3.23 (0.25–18.64)	4.02	4.59	3.12	11.08
Cl^- (μg m^{-3})	0.27 (0.00–2.11)	0.49	0.28	0.30	0.74
Na^+ (μg m^{-3})	0.06 (0.00–0.35)	0.04	0.08	0.06	0.12
K^+ (μg m^{-3})	0.18 (0.00–0.54)	0.22	0.26	0.11	0.23
Mg^{2+} (μg m^{-3})	0.01 (0.00–0.10)	0.00	0.00	0.04	0.04
Ca^{2+} (μg m^{-3})	0.07 (0.00–0.63)	0.04	0.05	0.22	0.18
OC^a (μg m^{-3})	3.70 (0.00–14.33)	4.33	5.65	4.09	7.18
EC^a (μg m^{-3})	1.26 (0.00–4.47)	1.36	1.91	1.41	2.77
O_3 (ppbv)	20 (1–65)	22	16	18	22
NO_2 (ppbv)	31 (6–78)	37	43	37	42
HONO (ppbv)	1.24 (0.00–6.17)	1.39	1.33	2.46	1.95
HNO_3 (ppbv)	0.13 (0.00–0.90)	0.09	0.42	0.07	0.13
NH_3 (ppbv)	6.52 (1.06–15.14)	7.92	8.57	7.89	8.49
$TVOCs^a$ (ppbv)	42.9 (7.5–118.9)	53.8	63.2	47.9	57.1
$PM_{2.5}/PM_{10}$	0.57 (0.16–1.00)	0.60	0.67	0.55	0.70
SO_4^{2-}/NO_3^-	0.79 (0.13–8.88)	0.57	0.58	0.29	0.32
OC/NO_3^-	1.17 (0.00–8.24)	1.21	0.69	0.59	0.30
NOR^a	0.07 (0.00–0.37)	0.09	0.08	0.10	0.21
SOR^a	0.17 (0.03–0.50)	0.17	0.26	0.13	0.34
NHR^a	0.33 (0.06–0.81)	0.35	0.41	0.35	0.58
$ALWC^{a,b}$ (μg m^{-3})	21.8 (0.1–395.9)	28.6	32.5	23.3	85.8
pH^b	3.37 (1.55–4.27)	3.42	3.38	3.81	3.64

[a] Abbreviations used in this study include temperature (T), wind speed (WS), relative humidity (RH), planetary boundary layer height (PBLH), organic carbon (OC), elemental carbon (EC), total volatile organic compounds (TVOCs), nitrogen oxidation ratio (NOR), sulfur oxidation ratio (SOR), ammonia conversion ratio (NHR) and aerosol liquid water content (ALWC). [b] These values were calculated using the ISORROPIA II model.

$PM_{2.5}$ mass was most strongly correlated with NO_3^- and NH_4^+, particularly when $PM_{2.5}$ concentrations exceeded 75 μg m^{-3}, whereas increases in SO_4^{2-}, OC and EC showed weaker correlations (Fig. 1 and Table S1). Among major constituents, the Pearson correlation coefficient was the highest between NO_3^- and NH_4^+, as expected (0.99). A previous study in Seoul reported that $PM_{2.5}$ concentrations were most strongly correlated with NH_4^+,[32] which was explained by the seasonal dominance of NO_3^- in winter and SO_4^{2-} in summer. In Fig. 1, the $PM_{2.5}$ mass was divided into six bins at 25 μg m^{-3} intervals for all four cases. $PM_{2.5}$ mass was also found to be strongly correlated with meteorological factors. Wind speed was the lowest when $PM_{2.5}$ and NO_3^- concentrations were high, and air temperature ranged from 10–15 °C, which was higher than the average during the measurement period.

3.2 Variation in $PM_{2.5}$ components and precursor gases

Throughout the measurement period, NO_3^- accounted for 31% of the major $PM_{2.5}$ components, SO_4^{2-} for 12% and NH_4^+ for 13%, with a combined contribution of 56%. Secondary inorganic aerosols are generally highly hygroscopic, absorbing moisture from the surrounding atmosphere and increasing ALWC. This process facilitates the transformation of acidic gases into the particle phase, leading to a rapid increase in NO_3^-, SO_4^{2-} and NH_4^+ concentrations, consequently elevating $PM_{2.5}$ levels.[5] In this study, ALWC generally increased with relative humidity and was higher during periods of elevated $PM_{2.5}$ concentration compared to the other periods. Notably, in Case 4, when the highest NO_3^- concentrations were observed, the average ALWC was 85.8 μg m^{-3} more than twice that of the other cases (Table 1). However, in this case, the precursor gas NO_2 was measured at 43 ppbv, which was lower than that in Case 2.

Additionally, aerosol ion formation is influenced by particle acidity. Along with NO_3^-, SO_4^{2-} and NH_4^+ establish an acid–base balance that determines aerosol pH. In winter, NO_3^- concentrations generally exceed SO_4^{2-}, leading to higher pH levels compared to summer when SO_4^{2-} dominates.[8] In the present study, pH values during high-$PM_{2.5}$ periods ranged from 3.0 to 4.0, suggesting that the aqueous oxidation pathway of SO_2 *via* hydrogen peroxide (H_2O_2) was dominant.[33,34] In contrast, haze episodes in Beijing rarely see a pH level drop below 4.0, typically remaining around 4.0–5.0.[35] These results imply that the atmospheric condition is relatively more acidic in Seoul, making it less favorable for NO_3^- production.

The $[NH_4^+]/[SO_4^{2-}]$ and $[NO_3^-]/[SO_4^{2-}]$ molar ratios exhibited a very strong linear correlation, indicating progressive neutralization: as nitrate accumulates, ammonium increases to retain charge balance (Fig. 2).[13,36] While the $[NO_3^-]/[SO_4^{2-}]$ ratios are higher under cold and humid conditions, when thermodynamics favor nitrate partitioning, ratios are lower in summer at higher temperature when sulfate becomes relatively more influential.[37–39] In this study, $PM_{2.5}$ concentrations increased with the $[NO_3^-]/[SO_4^{2-}]$ ratio, reaching the maximum at ratios of 5–8. In our previous study conducted in Beijing, $[NO_3^-]/[SO_4^{2-}]$ ratios were 1–3 in May and June 2016.[40] Episodes

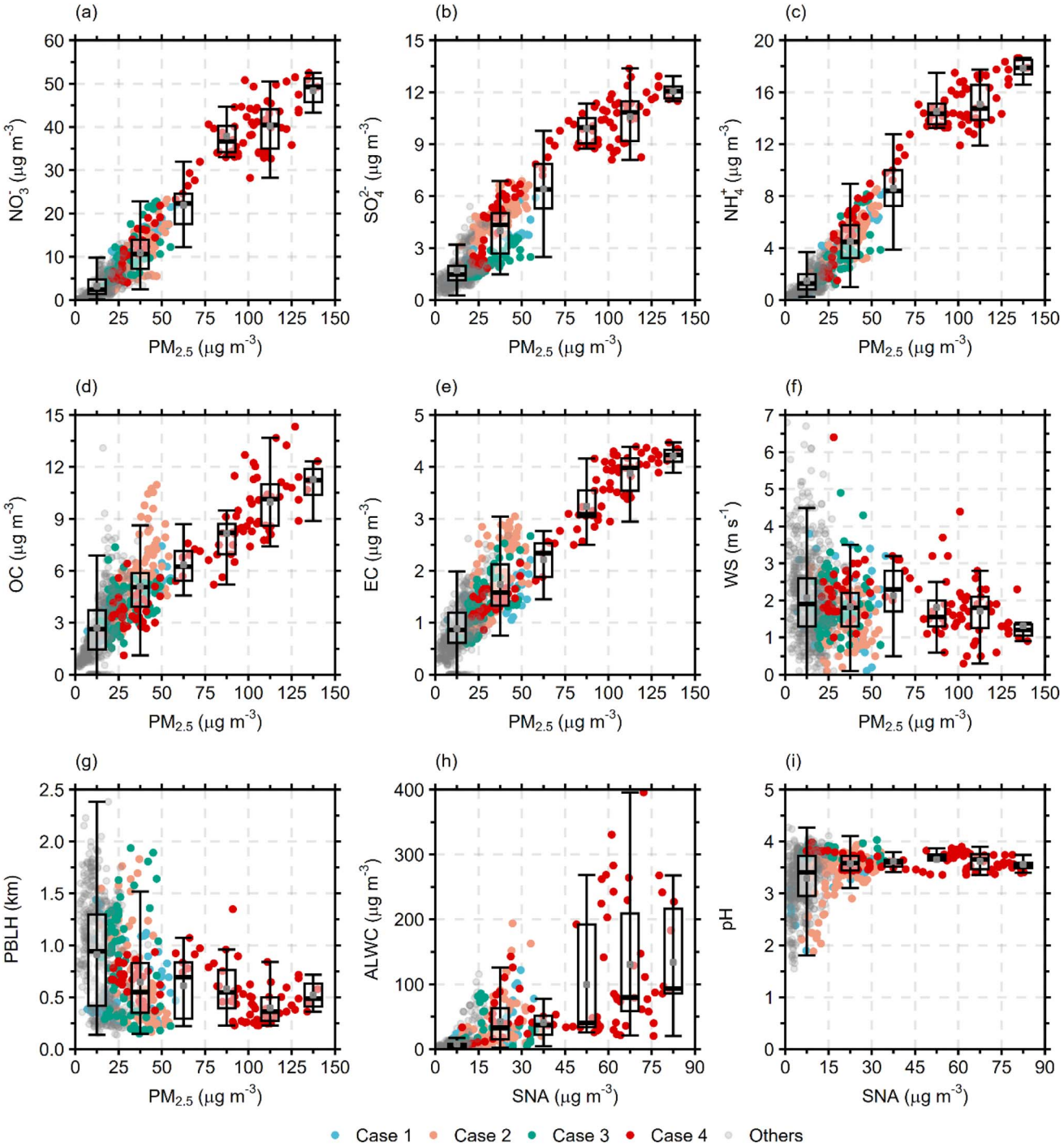

Fig. 1 Correlations of $PM_{2.5}$, its components and related variables during the measurement period. (a–e) Correlations between $PM_{2.5}$ concentrations and major $PM_{2.5}$ components. (f and g) Correlations with meteorological variables, including WS and PBLH. (h and i) Correlations between the sum of sulfate, nitrate and ammonium (SNA), ALWC and pH.

with elevated non-volatile cations (*e.g.*, Mg^{2+} and Ca^{2+}) in Case 3 show the highest ratios, consistent with mineral-dust nitrate formation (*e.g.*, calcium nitrate ($Ca(NO_3)_2$)) that increases nitrate *via* providing extra cations.[41]

For Cases 1–4, the NO_3^- concentration consistently increased with $PM_{2.5}$, with increases observed for the other major components. However, the concentrations of precursor gases exhibited less pronounced variations with $PM_{2.5}$. During the four cases, the air temperature and relative humidity were higher than the campaign average, while the wind speed and PBLH were lower (Table 1). Cases 1 and 3 (which were relatively short) had lower $PM_{2.5}$ concentrations, whereas Cases 2 and 4 (which were longer) had higher concentrations. In Case 1, the $PM_{2.5}$ concentration was briefly elevated from the afternoon of

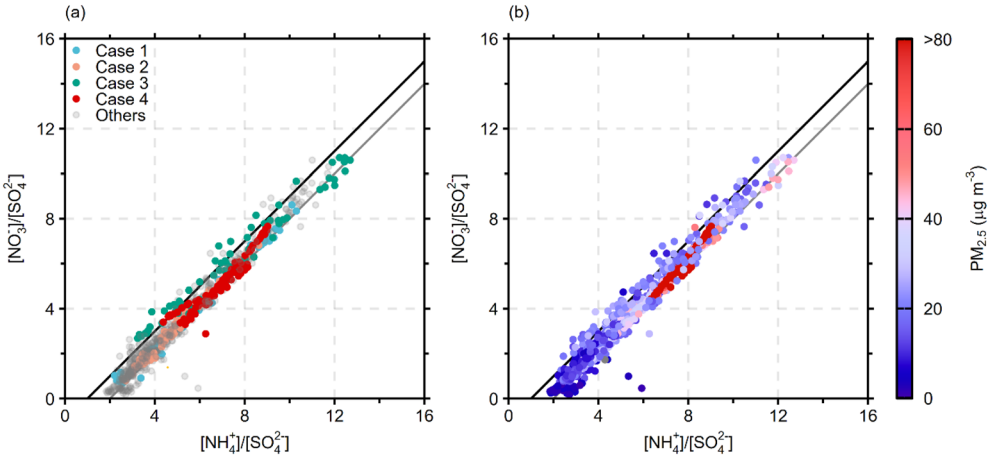

Fig. 2 Relationships between molar ratios of $[NH_4^+]/[SO_4^{2-}]$. (a) Data divided into four cases. (b) Data colored according to $PM_{2.5}$ concentration. The gray and black lines indicate theoretical $[NH_4^+]/[SO_4^{2-}]$ ratios of 2 : 1 and 1 : 1, respectively.

26 October to the morning of 27 October, when a low-level trough passed through, resulting in light precipitation and the lowest $PM_{2.5}$ concentration of the four cases. In Case 2, the $PM_{2.5}$ concentration slowly increased from 3 November and peaked on 5 November before decreasing until the end of the event. During this case, HNO_3 had a peak concentration about 3.2 times higher than the campaign average, while the NO_3^- concentration was generally lower than those in the other cases. In Case 3, the PM_{10} concentration was higher compared to $PM_{2.5}$, and the concentrations of cations such as Mg^{2+} and Ca^{2+} were about 3–4 times higher than the study average, possibly due to the influence of soil minerals. During this case, the HNO_3 concentration was the lowest observed during the campaign. Meanwhile, in Case 4, the concentrations of $PM_{2.5}$, PM_{10} and major $PM_{2.5}$ components were the highest observed during the campaign, with the following values (in μg m^{-3}): $PM_{2.5}$: 140, PM_{10}: 182, NO_3^-: 52.48, SO_4^{2-}: 13.37 and NH_4^+: 18.64.

3.3 Synoptic meteorological conditions during high-$PM_{2.5}$ events

This study was conducted during the monsoon transition period, which is characterized by the weakening of the North Pacific High and the development of Siberian High. This causes the periodic passage of cold fronts accompanied by migratory anticyclones.[42] Previous research showed that these frontal passages play a crucial role in transporting pollution as well as dust plumes from the Asian continent to the Northwest Pacific, particularly in spring. The soil minerals observed in Case 3 are transported from North China and Mongolia by frontal systems.[43] These systems lift pollutants above the boundary layer in their source regions, enabling long-range transport *via* low-level westerly winds.[44,45]

During the SIJAQ campaign, meteorological conditions typically changed over about a week, resulting in high-$PM_{2.5}$ events (Fig. S3). Therefore, these synoptic meteorological patterns were examined first. The daily variations in meteorological parameters are presented in Fig. 3. As shown in the figure, Seoul experienced a frontal passage every 3–4 days during the study period. During each high-$PM_{2.5}$ event, the passage of a weak trough generated between high-pressure systems was followed by increases in the sea surface pressure, temperature and relative humidity. Then, the $PM_{2.5}$ concentration increased, and the high-$PM_{2.5}$ events persisted for several days before finally ending with the arrival of rain brought by a strong trough. This reflects a typical characteristic of the periodic baroclinic system over the Korean Peninsula in monsoon transition periods, where high-$PM_{2.5}$ events are associated with frontal systems created by a continental high-pressure developing in the northwest and an anticyclone moving from the southwest. This pattern is especially evident in Cases 2 and 4, when $PM_{2.5}$ concentrations were significantly elevated compared to the campaign average. Detailed synoptic meteorological conditions are shown in the weather maps for Cases 2 and 4 (Fig. S3), illustrating the approach of the anticyclone and cold front system to the Korean Peninsula followed by the development of stagnant conditions. The daily backward air-mass trajectories for these two cases are shown in Fig. 4. These trajectories indicate that, during Case 2, air masses were transported from the Asian continent with an anticyclone system and stagnated under the high-pressure center positioned over the Korean Peninsula. In Case 4, the passage of the frontal system slowed down, and the stagnation effect did not reach the upper layers, resulting in a continued inflow in these layers.[45] In this case, the influence of the cold front led to a high cloud amount and a very low PBLH.

All four high-$PM_{2.5}$ events were accompanied by hazy and misty conditions (Fig. 3). The World Meteorological Organization (WMO) classifies fog as occurring when visibility is less than 1 km. Meanwhile, the KMA specifies that the relative humidity must exceed 90% for fog to occur. Conversely, mist is defined by the WMO as having a visibility between 1 and 10 km, and by the KMA as having a relative humidity above 80%. Additionally, mist is influenced by hydrometeors. Meanwhile, haze occurs when the relative humidity is 70% or lower and is caused by the presence of dry particles.[46] During winter, secondary inorganic aerosols are a key driver of severe $PM_{2.5}$

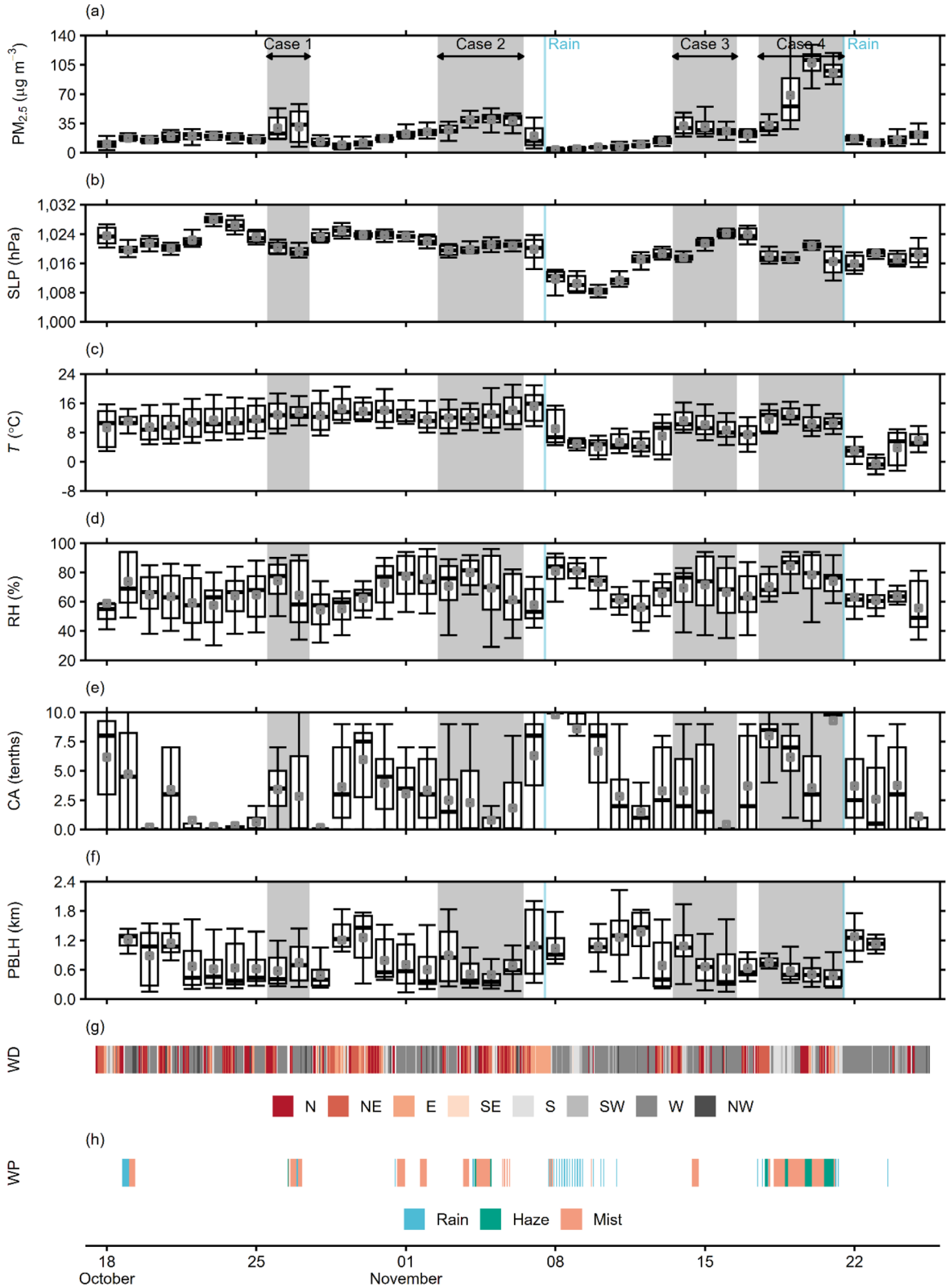

Fig. 3 Daily variations in $PM_{2.5}$ concentrations and meteorological factors. (a) $PM_{2.5}$ concentrations. (b–h) Meteorological factors including sea level pressure (SLP), temperature (*T*), cloud amount (CA), wind direction (WD) and weather phenomena (WP). WP is classified based on relative humidity and visibility.

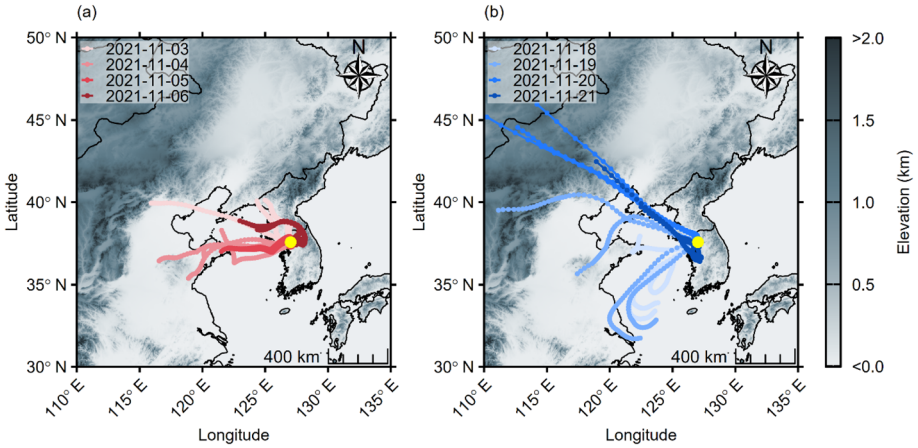

Fig. 4 Backward air-mass trajectories arriving in Seoul at 500 m altitude during high-$PM_{2.5}$ events. (a) Case 2. (b) Case 4.

pollution, suggesting that these relative humidity conditions are crucial in determining the composition of the particles and the occurrence of elevated $PM_{2.5}$ levels.

Although there were differences in the $PM_{2.5}$ concentrations, $PM_{2.5}$ chemical composition and meteorological factors between the four cases, common characteristics were evident compared to the average values for the study period, such as high relative humidity, high temperature and low wind speed (Table 1). These results confirm the previous finding that air quality in East Asia is significantly affected by synoptic conditions.[47] In a megacity such as Seoul, sources of fine particles in the city center, synoptic meteorological conditions, the boundary layer structure and atmospheric transport processes all play key roles in determining the concentration and type of pollutants.[48]

3.4 Evolution of major $PM_{2.5}$ components

The following discussion will focus on Cases 2 and 4, in which $PM_{2.5}$ mass concentrations were elevated for extended periods under distinct synoptic weather conditions, to explore the processes controlling the levels of NO_3^- in early winter in Seoul.

In these two cases, a significant increase in NO_3^- concentration was observed, while SO_4^{2-} and OC exhibited relatively smaller increases (Fig. 5). In Case 2, NO_3^- levels increased until noon on 5 November before declining, whereas SO_4^{2-} remained stable and OC gradually increased until 6 November. In Case 4, concentrations of all major $PM_{2.5}$ components increased on 19 November and remained relatively constant until 21 November. While NO_3^- exhibited dynamic variations, OC steadily increased during both events, reaching its peak in the latter half of each episode under highly stagnated conditions. This pattern was even more pronounced in precursor gases, such as NO_2 and TVOCs, compared to major $PM_{2.5}$ components and was more evident in Case 2 than in Case 4. Notably, in Case 2, NO_3^- variations were decoupled from NO_2, whereas OC variations closely correlated with TVOCs. Consequently, the OC/NO_3^- ratio was significantly higher in Case 2 than in Case 4 (Table 1) and increased in the latter half of the event compared to the earlier half (Fig. 5).

In both cases, elevated NO_3^- concentrations were the primary driver of high-$PM_{2.5}$ levels, whereas variations in SO_4^{2-} and OC played a lesser role. However, the mass ratios of the major $PM_{2.5}$ components differed significantly between the two cases. Fig. 6 presents ternary plots comparing the relative contributions of the three major components to $PM_{2.5}$ concentration in both cases. In a previous study conducted in central Seoul, the organic matter (OM) level was estimated to be 1.6 times that of the OC level.[49] In Case 4, the NO_3^- concentration increased significantly and remained high, resulting in a consistently elevated NO_3^- mass ratio. The mass ratios of SO_4^{2-} and OM remained stable throughout the episode.

In contrast, in Case 2, the relative abundances of NO_3^-, SO_4^{2-} and OM in $PM_{2.5}$ varied dynamically throughout the event. As $PM_{2.5}$ concentrations increased, both the concentration and mass ratio of NO_3^- increased, leading to distinct day–night differences. During the daytime, as O_3 levels increased and $PM_{2.5}$ concentrations decreased, the NO_3^- mass ratio declined, while SO_4^{2-} and OM mass ratios increased to approximately 40% and 60%, respectively. This pattern suggests that NO_3^- was likely subject to evaporation due to its volatility, driven by rising temperature and acidity. In conjunction with variations in $PM_{2.5}$ components and precursor gases discussed above, this analysis highlights the key differences in NO_3^- enhancement between the two cases: in Case 2, the $PM_{2.5}$ composition was more strongly influenced by local emissions and photochemical reactions than in Case 4.

To diagnose gas-to-particle conversion processes, the nitrogen oxidation ratio (NOR), sulfur oxidation ratio (SOR) and ammonia conversion ratio (NHR) are commonly used. They are defined as follows:

$$NOR = [NO_3^-]/([NO_3^-] + [NO_2]) \quad (1)$$

$$SOR = [SO_4^{2-}]/([SO_4^{2-}] + [SO_2]) \quad (2)$$

$$NHR = [NH_4^+]/([NH_4^+] + [NH_3]) \quad (3)$$

Theoretically, these ratios are influenced equally by gaseous precursors and aerosol particles. In this study, all ratios tended to increase with NO_3^- levels and were significantly higher in Case 4, where the conversion ratio scaled proportionally with particulate-

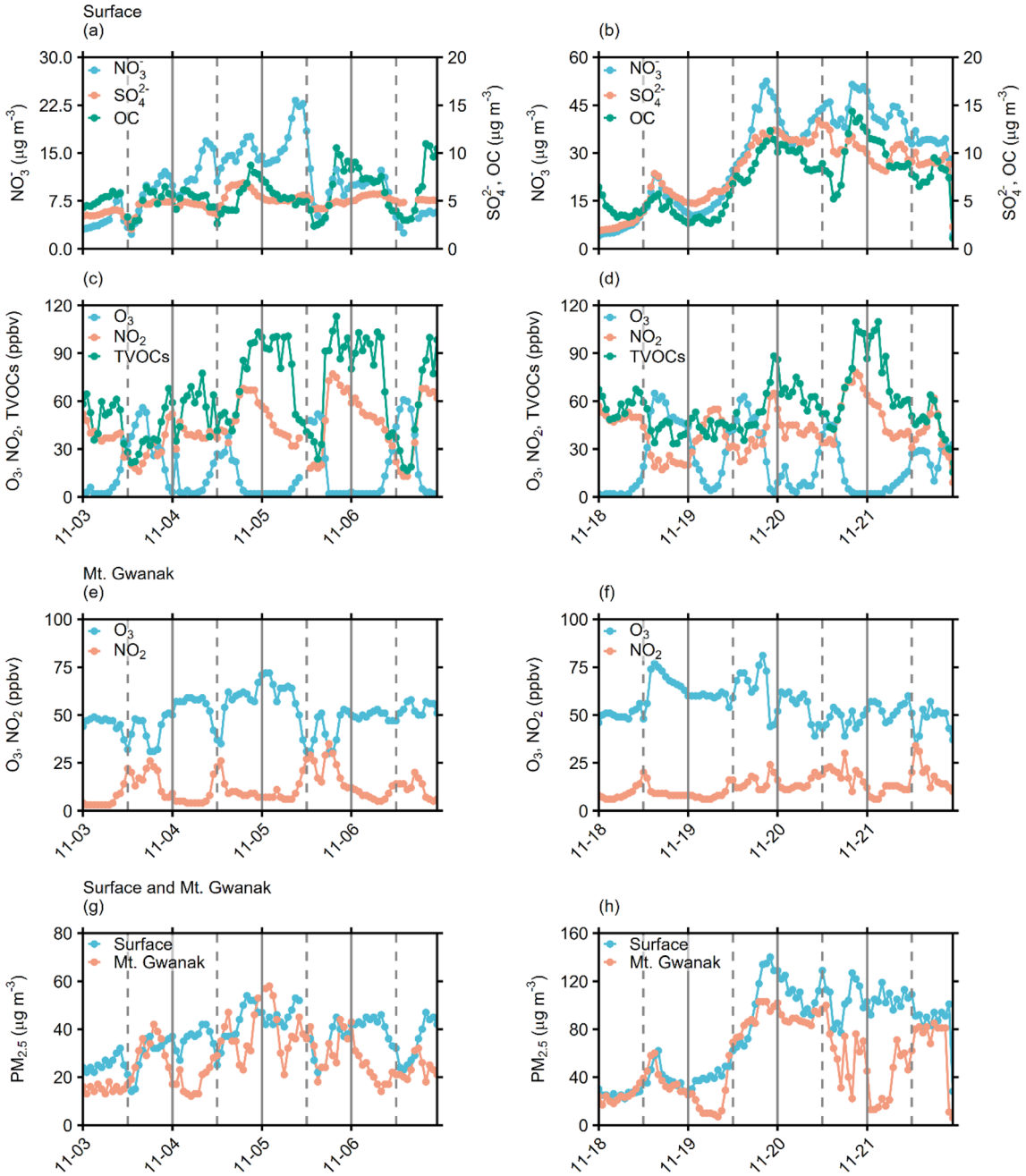

Fig. 5 Hourly variations of $PM_{2.5}$ components and gaseous species during Cases 2 and 4. The left and right columns show Cases 2 and 4, respectively. (a–d) Surface-level concentrations of NO_3^-, SO_4^{2-}, OC, O_3, NO_2 and TVOCs. (e and f) O_3 and NO_2 concentrations measured at the summit of Mt. Gwanak. (g and h) $PM_{2.5}$ concentrations at the surface (Dongdaemun-gu site) and at the summit of Mt. Gwanak.

phase concentrations. Although NO_3^- and NO_2 concentrations are typically high in winter, NOR remained the lowest among the three ratios and varied within a narrow range (Table 1). These results highlight the limitations of using conversion ratios to trace the formation mechanism of secondary inorganic aerosols.

3.5 Increase in nitrate levels in relation to thermodynamic equilibrium

Particulate NO_3^- is commonly evaluated using thermodynamic equilibrium (reaction (R3)), with gas–particle partitioning controlled by the temperature-dependent solid product (K_p) of HNO_3 and NH_3 and DRH of NH_4NO_3:[14,16,50,51]

$$\ln(K_p) = 84.6 - 24\,220/T - 6.1\ln(T/298.15) \quad (4)$$

$$\ln(\mathrm{DRH}) = 723.7/T + 1.7037 \quad (5)$$

The theoretical K_p calculated using eqn (4) is compared with the product of ambient HNO_3 and NH_3 mixing ratios for Cases 2 and 4 (Fig. 7). If the ambient products exceed saturation values, *i.e.*, if the measurement points are positioned above the

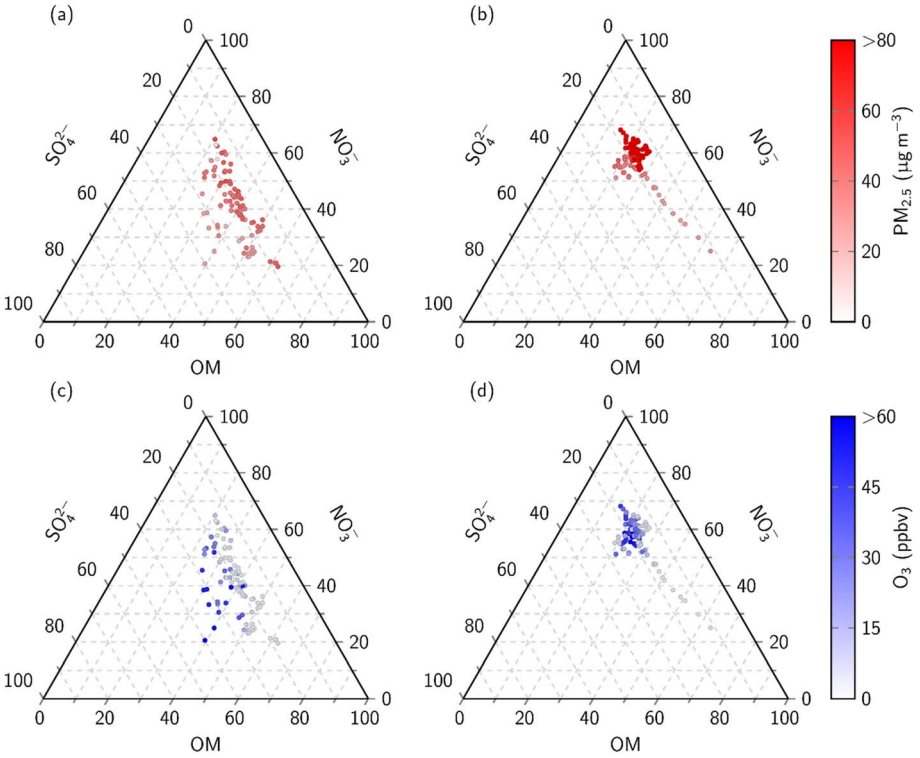

Fig. 6 Relative composition of NO_3^-, SO_4^{2-} and OM during Cases 2 and 4. The left and right columns show Cases 2 and 4, respectively. (a and b) Ternary plots showing the relative fractions of NO_3^-, SO_4^{2-} and OM in $PM_{2.5}$, colored by $PM_{2.5}$ concentration. (c and d) Ternary plots, colored by O_3 concentration.

equilibrium line, NH_4NO_3 particles can form and subsequently transform into NO_3^- under ambient relative humidity conditions greater than DRH. Although HNO_3 lag-related bias cannot be fully excluded, our inlet configuration and sampling height likely minimized adsorption losses. Therefore, K_p analysis is used here as a regime-level diagnostic rather than strict instantaneous thermodynamic closure.[52] Similar to the relative chemical composition of $PM_{2.5}$ shown in Fig. 6, the thermodynamic conditions for NO_3^- differed significantly between the two cases. In Case 4, the ambient product mostly exceeded saturation levels and varied along the equilibrium line. In contrast, in Case 2, the ambient product varied more drastically, being either much higher or much lower than the saturation levels. Additionally, NO_3^- concentrations were significantly higher in Case 4, despite the higher ambient products observed in Case 2.

In Case 2, nighttime measurements were positioned to the right of the equilibrium line in Fig. 7, while daytime measurements shifted to the left. During the daytime, relative humidity was also much lower than DRH (Fig. S4). This suggests that NH_4NO_3 was likely formed and NO_3^- accumulated at night under low temperatures and high relative humidity but tended to evaporate during the day, coinciding with an increased mass ratio of SO_4^{2-}. In contrast, in Case 4, the products of ambient precursors, mostly exceeding saturation levels, were aligned along the equilibrium line. Once NO_3^- concentrations began to increase, they remained consistently high with only slight variations throughout the day and night. Therefore, it is likely that air masses carrying high $PM_{2.5}$ were transported to and remained over the Korean Peninsula under stable atmospheric conditions (Fig. 4). Consequently, local influences were not significant enough to alter the regional characteristics of the air mass.

The distinct chemical characteristics of the two high-NO_3^- events highlight the strong dependence of NO_3^- levels on meteorological conditions, which influence both the formation mechanism and dominant sources. Case 2 occurred under the influence of a persistent anticyclone, during which NO_3^- gradually increased, and the $PM_{2.5}$ composition varied in response to local variations in precursor gases under stagnant conditions. On the other hand, NO_3^- levels increased rapidly due to continental outflows associated with the passage of the frontal system. In the latter half of the episode, changes in $PM_{2.5}$ composition were relatively minor compared to the background levels under highly stable atmospheric conditions. Therefore, the following sections will examine key atmospheric agents affecting NO_3^-, such as pre-existing particles and boundary layer height, in greater detail.

3.6 Increase in nitrate levels in relation to pre-existing particles

In an equilibrium framework, particulate NO_3^- is controlled by precursor levels, temperature and relative humidity. However, as shown in Fig. 7, the observed NO_3^- variability does not always follow these thermodynamic constraints alone. Because HNO_3 is highly soluble and surface-reactive, it can be efficiently

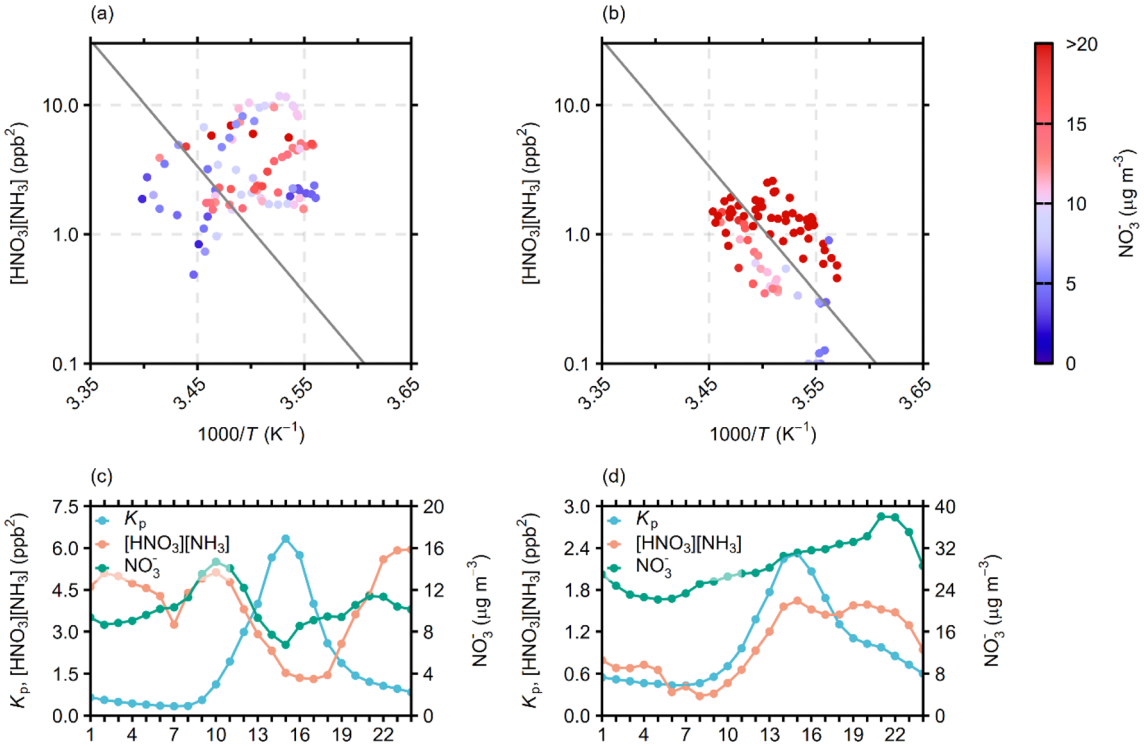

Fig. 7 Comparison of the product of HNO_3 and NH_3 with the equilibrium constant K_p during Cases 2 and 4. The left and right columns show Cases 2 and 4, respectively. (a and b) The product of HNO_3 and NH_3 is compared with K_p for the NH_4NO_3 gas–particle partitioning system, calculated at the corresponding temperatures (solid line). (c and d) Diurnal variations of K_p, product of HNO_3 and NH_3 and the NO_3^- concentration.

taken up by and absorbed onto pre-existing aerosol surfaces or dissolved into aqueous droplets. During high-$PM_{2.5}$ events, the nighttime pathway of HNO_3 *via* dinitrogen pentoxide (N_2O_5) hydrolysis often dominates NO_3^- production under high relative humidity with abundant droplet-mode particles (reaction (R6)).[8] Once produced, HNO_3 partitions to the particle phase when NH_3 is sufficient.[53] Fig. 2 indicates that particles were fully neutralized by NH_4^+, implying that NH_3 was not limiting in the study region.

Moreover, NO_3^- varied in phase with the droplet mode (Fig. 8), implicating gas–aqueous partitioning as the dominant control on particulate NO_3^-. This points to particle surface area and liquid water as key enablers of rapid $PM_{2.5}$ increases. Fig. 8 further resolves the size distribution into Aitken (<0.1 μm), condensation (0.1–0.5 μm) and droplet (0.5–1.0 μm) modes: typically associated with maxima in number, surface and volume of aerosol particles, respectively. While Aitken-mode particles are likely dominated by locally emitted black carbon (BC),[54] the condensation and droplet modes provide surface and aqueous volume that facilitate NO_3^- partitioning[13] and, in the case of the droplet mode, rapid aqueous-phase production of NO_3^-.[55]

It is also evident that the daily evolution of boundary layer height significantly influences both particle and NO_3^- distributions. While NO_3^- concentrations gradually increased in Case 2, they exhibited a smaller fluctuation after a rapid initial rise in Case 4, typically increasing during the morning and nighttime but decreasing during the day, which is attributed to the expansion of PBLH. In both cases, air masses became highly stagnant in the latter half of the events. Consequently, the boundary layers expanded significantly in Case 2 under a persistent anticyclonic system, whereas the development of the mixing layer in Case 4 was suppressed by a thick cloud associated with a frontal system. For this reason, the number concentrations of nanoparticles exhibited distinct diurnal variations with two daily peaks, and the elevated NO_3^- levels in Case 2 were rapidly dissipated with the development of the boundary layer on 5 November. In contrast, in Case 4, the increase in NO_3^- coincided with expansion of the boundary layer. The initial rise was associated with an increase in the surface areas of condensation-mode particles during the day on 19 November, followed by an increase in the volume concentrations of droplet-mode particles on the following days, 20 and 21 November. Note that the number concentrations of nanoparticles remained low in this case.

In the four observed cases, the concentrations of droplet-mode particles increased, primarily at night, but also during the late morning when the boundary layer expanded. In contrast, the number concentrations of Aitken-mode particles tended to increase in the morning hours, which was pronounced during Case 4.

In urban environments, BC particles provide surfaces for reactions. Previous studies have demonstrated that the production of secondary inorganic aerosols is closely linked to the coating thickness of BC particles.[56,57] In Seoul, the average diameter of the BC core is typically around 100 nm or smaller, and condensable gases such as HNO_3 and sulfuric acid (H_2SO_4)

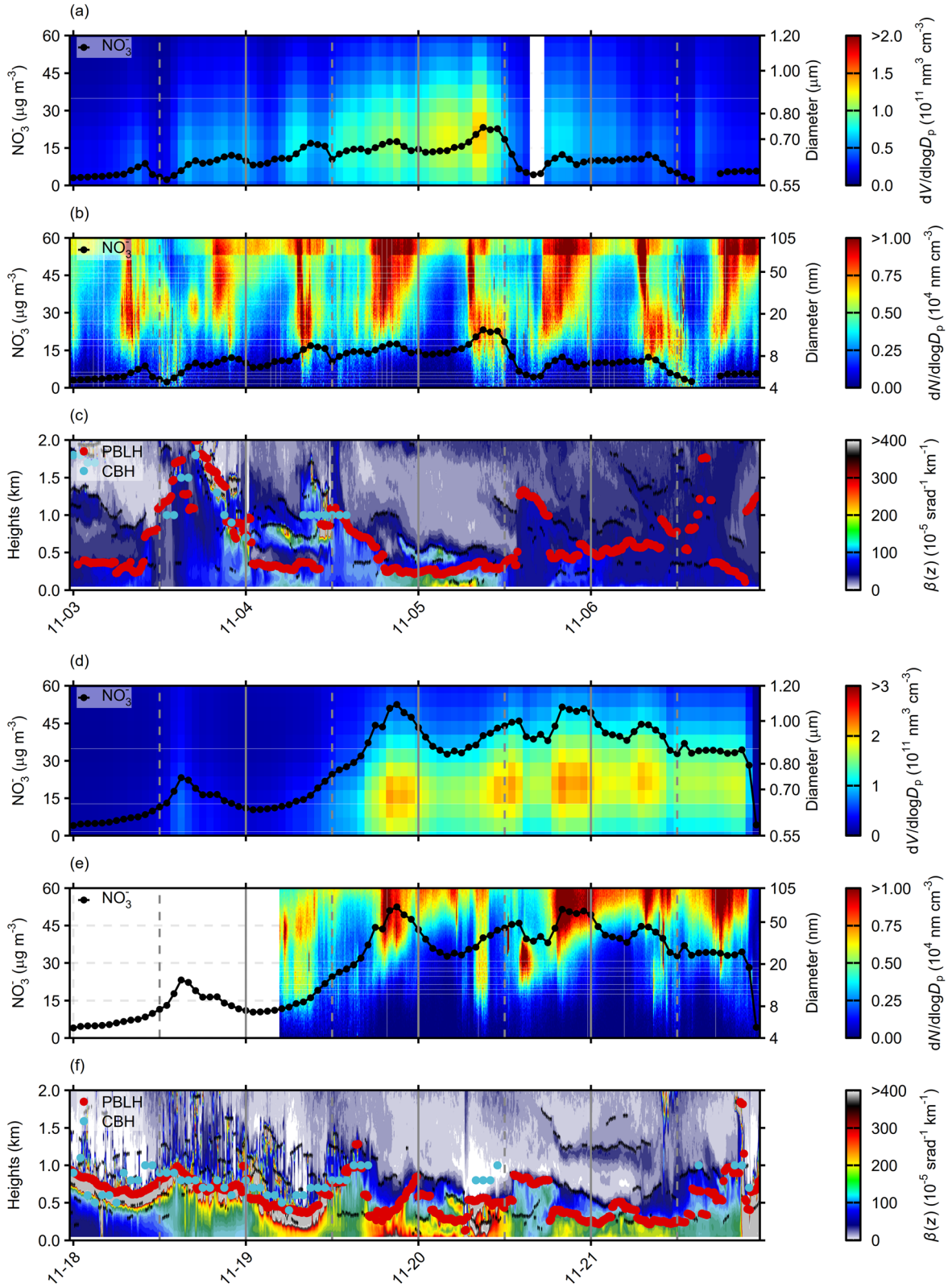

Fig. 8 Size-resolved distributions of aerosol particle properties during Cases 2 and 4. (a–c) Size-resolved distributions of aerosol particle number and volume concentrations, as well as backscattering coefficients, overlaid with NO_3^-, PBLH and cloud base height (CBH) for Case 2. (d–f) Same variables for Case 4. (c and f) Black dots indicate PBLH estimated by the five methods.

can contribute to their growth by forming coatings, often leading to particle sizes exceeding 400 nm during long-range transport.[56,58,59] The growth rate of BC particles typically progresses at a few nanometers per hour.[54] In Case 2, both droplet-mode and Aitken-mode particles exhibited reasonable correlations with NO_3^- concentrations, especially during nighttime and early morning hours, suggesting the contribution of particulate NO_3^- formation under thermodynamically favorable conditions. Chamber experiments have shown that NO_3^- can be generated *via* heterogeneous reactions involving high concentrations of O_3 and NO_2 within the moisture layers surrounding BC particles at high relative humidity (90%).[58]

Although surface O_3 concentrations were generally low at night in Case 2, O_3 levels remained relatively elevated in Case 4, particularly during the early nighttime period. This may reflect the influence of prevailing southwesterly winds in Case 4, which likely transported O_3-rich air masses from the Yellow Sea into Seoul. The formation of nitrate radical (NO_3) and N_2O_5 near the surface is plausible under humid conditions when O_3-rich marine air mixes with NO_x-rich urban air. However, elevated NO_x concentrations likely suppressed NO_3 accumulation through rapid titration,[60] indicating an atmospheric environment unfavorable for sustained N_2O_5 formation. Additionally, previous studies have shown that NO_3 and N_2O_5 concentrations tend to increase significantly only under conditions involving vertical mixing between surface and upper layers.[60] Given that the PBLH remained low and stable during nighttime across these events, it is unlikely that the observed high-NO_3^- concentrations were driven primarily by local oxidation of NO_x by O_3.[61] Moreover, in Case 4, the chemical composition of $PM_{2.5}$ showed little variation between day and night, and NO_3^- remained near thermodynamic equilibrium with the gas-phase precursors. These findings suggest that local oxidation processes, including N_2O_5 hydrolysis, were not the dominant contributors to the observed high-NO_3^- enhancements.

Additionally, the number concentrations of droplet-mode particles increased during the daytime expansion of the boundary layer. The concentration of nanoparticles is typically elevated during new particle formation (NPF) events, and boundary layer expansion has been proposed as a key mechanism facilitating vertical mixing that supports such events.[50] In this study, both nanoparticle and droplet-mode particle concentrations increased with boundary layer expansion. This suggests that the daytime increase in accumulation-mode particles was likely driven by the photochemical production of HNO_3 and its subsequent partitioning into the particle phase. In Case 2, this process was likely associated with the upward transport of locally emitted precursors, whereas in Case 4, it was influenced by the entrainment of upper-layer continental outflows. This entrainment introduced aged particles into the boundary layers during its expansion, particularly under conditions of initially shallow PBL.

3.7 Increase in nitrate levels in relation to the PBLH

At the summit of Mt. Gwanak (632 m a.s.l.) in southwestern Seoul (Fig. S1), criteria pollutants including $PM_{2.5}$, O_3 and NO_2 concentrations have been measured since 2018 by SIHE. For the two cases, measurements of reactive gases and $PM_{2.5}$ at mountain summit were analyzed in relation to variations in PBLH. Their diurnal variations are closely linked with the evolution of PBLH.

At Mt. Gwanak, NO_x, a representative indicator of urban emissions, generally increases as the PBL expands and decreases as the PBL collapses, remaining low at night when Mt. Gwanak is above the PBL. Similarly, the $PM_{2.5}$ mass concentration increased during the day and decreased at night. In contrast, O_3 remained elevated overnight but declined in the morning as NO_x levels increased. However, the diurnal variation of O_3 exhibits a peak when the PBL is fully developed, coinciding with the O_3 peak observed at the surface. This indicates that the Mt. Gwanak site is influenced by the urban air masses during the daytime, whereas nighttime conditions are characterized by outflow air. Furthermore, the distinct variations associated with PBL dynamics demonstrate that the upward transport of primary pollutants and the downward mixing of secondary pollutants, driven by the diurnal evolution of PBL, play a crucial role in conveying urban emissions into free troposphere, where the photochemical O_3 production is enhanced.

During the two events, O_3 and NO_2 showed opposite trends in the first half of each event. In Case 2, O_3 progressively increased as an anticyclone system approached, whereas in Case 4, elevated O_3 levels declined with increasing NO_2 concentrations. In the latter half of both events, O_3 and NO_2 concentrations stabilized due to air stagnation, accompanied by elevated TVOCs at the surface (Fig. 5). In contrast, the $PM_{2.5}$ mass concentration displayed markedly different patterns between the two cases, particularly when comparing measurements at the surface and aloft. In Case 2, $PM_{2.5}$ variations at both sites were generally in phase, except at night when surface $PM_{2.5}$ concentrations were significantly higher. In Case 4, however, a simultaneous increase in $PM_{2.5}$ was observed at both the surface and aloft sites in the first half of the event, indicating a more synchronized increase in $PM_{2.5}$ throughout the atmospheric column.

In the latter half of both events, surface $PM_{2.5}$ increased twice daily, once in the morning as the boundary layer expanded and again in the evening as it contracted. At the Mt. Gwanak site, the daytime increase was more consistently observed. In Case 2, $PM_{2.5}$ mass rapidly decreased with PBL expansion on 5 November, likely due to the dilution and dissipation of secondary inorganic aerosols (Fig. 5). However, the increase in $PM_{2.5}$ during PBL expansion is difficult to explain without considering active processes. Furthermore, the rapid increase in droplet-mode particle concentrations during PBL expansion suggests that physical mechanisms, rather than *in situ* chemical formation, played a dominant role in the observed $PM_{2.5}$ enhancements. A detailed analysis of meteorological conditions during the SIJAQ campaign revealed that the upper boundary layer is influenced by geostrophic winds, which facilitate the horizontal transport of particles.[45] Consequently, the daytime increase in $PM_{2.5}$ concentrations observed in Case 4 may have been driven by the expansion of the PBL, facilitating

entrainment and subsequent downward mixing of long-range transported pollutants from the upper atmosphere.

Another contributing factor could be the interaction between aerosols in low stratus clouds and $PM_{2.5}$ within the mixing layer as the PBL expands.[62] On 19 November, a rapid increase in droplet-mode particle numbers and NO_3^- concentrations was observed at the surface, coinciding with PBL expansion and cloud dissipation (Fig. 8). This suggests that aerosols initially incorporated into the cloud during vertical mixing may have been retained in the mixing layer as the cloud dissipated, contributing to the observed increase in $PM_{2.5}$; however, further evidence is needed to confirm this process.

4 Conclusions

This study analyzed four early-winter $PM_{2.5}$ pollution events in Seoul and identified NO_3^- as the primary driver of elevated $PM_{2.5}$ mass. Among these, two representative cases (Cases 2 and 4) highlighted contrasting formation mechanisms under different synoptic meteorological conditions.

Under anticyclone (Case 2), limited vertical mixing enabled the nighttime accumulation of NO_3^- *via* thermodynamically favorable gas-to-particle conversion, while daytime evaporation was promoted by rising temperature and aerosol acidity. In contrast, the cold frontal passage in Case 4 sustained NO_3^- enhancement through regional transport and vertical entrainment, retaining elevated levels both day and night.

Thermodynamic analysis confirmed that ammonium nitrate formation was favored across most events, with ambient precursor concentrations frequently exceeding equilibrium thresholds. The growth of droplet-mode particles coincided with NO_3^- accumulation, indicating condensation onto pre-existing aerosols. Boundary layer dynamics further modulated surface concentrations: in Case 2, daytime boundary layer expansion diluted NO_3^- levels, whereas in Case 4, it facilitated downward mixing of aged, nitrate-rich aerosols.

These findings underscore the multifaceted drivers of winter haze in East Asian megacities, emphasizing the critical role of synoptic meteorology, thermodynamic conditions and aerosol microphysics. Effective mitigation strategies must therefore combine targeted emission controls with meteorologically informed forecasting to manage severe $PM_{2.5}$ pollution episodes.

This one-month, high-NO_x case study is subject to near-surface dry-deposition bias and to equilibrium assumptions in ISORROPIA II, and it cannot fully separate synoptic transport from local formation. Future work should include vertical observations, broader precursor speciation and integrated modeling.

Author contributions

H. L. conducted the formal analysis and investigation, validated the results and was responsible for visualization and writing of the original draft. M. L. conceptualized the study, acquired funding and resources, supervised the project and contributed to the review and editing of the manuscript. S. L. also supervised the project and contributed to the review and editing. L.-S. C. administered the project. K. K., Y. C. and M.-S. P. provided resources. J. G., J.-A. K. and C. Y. contributed to the investigation and validation.

Conflicts of interest

There are no conflicts to declare.

Data availability

The data supporting the findings of this study are available in the article and its supplementary information (SI). Additional data in alternative formats are available from the corresponding author upon reasonable request. Supplementary information is available. See DOI: https://doi.org/10.1039/d5em00589b.

Acknowledgements

This work was supported by a grant from the National Institute of Environmental Research (NIER) funded by the Ministry of Environment (ME) of South Korea (NIER-2021-04-02-085 and NIER-2023-04-02-089) and National Research Foundation of Korea supported by the Ministry of Science and ICT (RS-2025-00573406). S. L. would like to thank Chungnam National University for its support (2023-0560-01).

References

1 M. M. Haque, K. Kawamura, D. K. Deshmukh, C. Fang, W. Song, B. Mengying and Y.-L. Zhang, Characterization of organic aerosols from a Chinese megacity during winter: predominance of fossil fuel combustion, *Atmos. Chem. Phys.*, 2019, **19**, 5147–5164.
2 J. Nirmalkar, J. Jung, S. Han, Z. Dong, Z. Xu, P. Fu and C. M. Pavulari, Chemistry of $PM_{2.5}$ in haze events in two East Asian cities during winter–spring 2019, *Atmos. Environ.*, 2023, **293**, 119457.
3 Z.-Y. Chen, H. Petetin, R. F. M. Turrubiates, H. Achebak, C. P. García-Pando and J. Ballester, Population exposure to multiple air pollutants and its compound episodes in Europe, *Nat. Commun.*, 2024, **15**, 2094.
4 H. Wang, Y. Zhang, H. Zhao, X. Lu, Y. Zhang, W. Zhu, C. P. Nielsen, X. Li, Q. Zhang, J. Bi and M. B. McElroy, Trade-driven relocation of air pollution and health impacts in China, *Nat. Commun.*, 2017, **8**, 738.
5 J. Su, P. Zhao, S. Ge and J. Ding, Aerosol liquid water content of $PM_{2.5}$ and its influencing factors in Beijing, China, *Sci. Total Environ.*, 2022, **839**, 156342.
6 S. Zhai, D. J. Jacob, X. Wang, Z. Liu, T. Wen, V. Shah, K. Li, J. M. Moch, K. H. Bates, S. Song, L. Shen, Y. Zhang, G. Luo, F. Yu, Y. Sun, L. Wang, M. Qi, J. Tao, K. Gui, H. Xu, Q. Zhang, T. Zhao, Y. Wang, H. C. Lee, H. Choi and H. Liao, Control of particulate nitrate air pollution in China, *Nat. Geosci.*, 2021, **14**, 389–395.
7 X. Sun, R. Zhang and G. Wang, Spatial-temporal evolution of health impact and economic loss upon exposure to $PM_{2.5}$ in China, *Int. J. Environ. Res. Public Health*, 2022, **19**, 1922.

8 S. Lim, M. Lee, J. Savarino and P. Laj, Oxidation pathways and emission sources of atmospheric particulate nitrate in Seoul: based on $\delta^{15}N$ and $\Delta^{17}O$ measurements, *Atmos. Chem. Phys.*, 2022, **22**, 5099–5115.

9 National Institute of Environmental Research (NIER), *Annual Report of Air Quality in Korea 2021*, NIER, Incheon, South Korea, 2022.

10 National Institute of Environmental Research (NIER), *2021 Annual Report of Air Quality Research Center*, NIER, Incheon, South Korea, 2022.

11 U. Mehmood and A. Mansoor, CO_2 emissions and the role of urbanization in East Asian and Pacific countries, *Environ. Sci. Pollut. Res.*, 2021, **28**, 58549–58557.

12 S. S. Brown and J. Stutz, Nighttime radical observations and chemistry, *Chem. Soc. Rev.*, 2012, **41**, 6405–6447.

13 J. H. Seinfeld and S. N. Pandis, *Atmospheric Chemistry and Physics: from Air Pollution to Climate Change*, John Wiley & Sons, Inc., Hoboken, NJ, USA, 3rd edn, 2016.

14 M. Wang, W. Kong, R. Marten, X.-C. He, D. Chen, J. Pfeifer, A. Heitto, J. Kontkanen, L. Dada, A. Kürten, T. Yli-Juuti, H. E. Manninen, S. Amanatidis, A. Amorim, R. Baalbaki, A. Baccarini, D. M. Bell, B. Bertozzi, S. Bräkling, S. Brilke, L. C. Murillo, R. Chiu, B. Chu, L.-P. De Menezes, J. Duplissy, H. Finkenzeller, L. G. Carracedo, M. Granzin, R. Guida, A. Hansel, V. Hofbauer, J. Krechmer, K. Lehtipalo, H. Lamkaddam, M. Lampimäki, C. P. Lee, V. Makhmutov, G. Marie, S. Mathot, R. L. Mauldin, B. Mentler, T. Müller, A. Onnela, E. Partoll, T. Petäjä, M. Philippov, V. Pospisilova, A. Ranjithkumar, M. Rissanen, B. Rörup, W. Scholz, J. Shen, M. Simon, M. Sipilä, G. Steiner, D. Stolzenburg, Y. J. Tham, A. Tomé, A. C. Wagner, D. S. Wang, Y. Wang, S. K. Weber, P. M. Winkler, P. J. Wlasits, Y. Wu, M. Xiao, Q. Ye, M. Zauner-Wieczorek, X. Zhou, R. Volkamer, I. Riipinen, J. Dommen, J. Curtius, U. Baltensperger, M. Kulmala, D. R. Worsnop, J. Kirkby, J. H. Seinfeld, I. El-Haddad, R. C. Flagan and N. M. Donahue, Rapid growth of new atmospheric particles by nitric acid and ammonia condensation, *Nature*, 2020, **581**, 184–189.

15 W. Zhou, W. Xu, H. Kim, Q. Zhang, P. Fu, D. R. Worsnop and Y. Sun, A review of aerosol chemistry in Asia: insights from aerosol mass spectrometer measurements, *Environ. Sci.: Processes Impacts*, 2020, **22**, 1616–1653.

16 A. Hrdina, J. G. Murphy, A. G. Hallar, J. C. Lin, A. Moravek, R. Bares, R. C. Petersen, A. Franchin, A. M. Middlebrook, L. Goldberger, B. H. Lee, M. Baasandorj and S. S. Brown, The role of coarse aerosol particles as a sink of HNO_3 in wintertime pollution events in the Salt Lake Valley, *Atmos. Chem. Phys.*, 2021, **21**, 8111–8126.

17 M. M. Twigg, A. J. C. Berkhout, N. Cowan, S. Crunaire, E. Dammers, V. Ebert, V. Gaudion, M. Haaima, C. Häni, L. John, M. R. Jones, B. Kamps, J. Kentisbeer, T. Kupper, S. R. Leeson, D. Leuenberger, N. O. B. Lüttschwager, U. Makkonen, N. A. Martin, D. Missler, D. Mounsor, A. Neftel, C. Nelson, E. Nemitz, R. Oudwater, C. Pascale, J.-E. Petit, A. Pogany, N. Redon, J. Sintermann, A. Stephens, M. A. Sutton, Y. S. Tang, R. Zijlmans, C. F. Braban and B. Niederhauser, Intercomparison of *in situ* measurements of ambient NH_3: instrument performance and application under field conditions, *Atmos. Meas. Tech.*, 2022, **15**, 6755–6787.

18 J. Ding, P. Zhao, J. Su, Q. Dong, X. Du and Y. Zhang, Aerosol pH and its driving factors in Beijing, *Atmos. Chem. Phys.*, 2019, **19**, 7939–7954.

19 N.-K. Kim, Y.-P. Kim, H.-J. Shin and J.-Y. Lee, Long-term trend of the levels of ambient air pollutants of a megacity and a background area in Korea, *Appl. Sci.*, 2022, **12**, 4039.

20 Y. Pan, S. Tian, Y. Zhao, L. Zhang, X. Zhu, J. Gao, W. Huang, Y. Zhou, Y. Song, Q. Zhang and Y. Wang, Identifying ammonia hotspots in China using a national observation network, *Environ. Sci. Technol.*, 2018, **52**, 3926–3934.

21 A. A. Nair and F. Yu, Quantification of atmospheric ammonia concentrations: a review of its measurement and modeling, *Atmosphere*, 2020, **11**, 1092.

22 Y. Liu, J. Zhan, F. Zheng, B. Song, Y. Zhang, W. Ma, C. Hua, J. Xie, X. Bao, C. Yan, F. Bianchi, T. Petäjä, A. Ding, Y. Song, H. He and M. Kulmala, Dust emission reduction enhanced gas-to-particle conversion of ammonia in the North China Plain, *Nat. Commun.*, 2022, **13**, 6887.

23 C. Ren, X. Huang, T. Liu, Y. Song, Z. Wen, X. Liu, A. Ding and T. Zhu, A dynamic ammonia emission model and the online coupling with WRF–Chem (WRF–SoilN–Chem v1.0): development and regional evaluation in China, *Geosci. Model Dev.*, 2023, **16**, 1641–1659.

24 S. Lim, M.-S. Bae, J. Jang, A. K. Dwivedi, J. Gil, J. A. Kim, M. Lee, S.-H. Oh, S.-A. Shin and L.-S. Chang, Exploring fine-aerosol episodes in urban Seoul during the cold season of the 2021 SIJAQ campaign: measurement evidences of heterogeneous reactions on black carbon particles, *Atmos. Environ.*, 2025, **342**, 120926.

25 S. Kang, J.-A. Kim, M. Lee, J. Park, E. Jeon, M. Shim and Y. Shin, An analysis of the temporal variability in volatile organic compounds (VOCs) within megacity Seoul and an identification of their sources, *Atmos. Pollut. Res.*, 2022, **13**, 101338.

26 J.-S. Min, M.-S. Park, J.-H. Chae and M. Kang, Integrated System for Atmospheric Boundary Layer Height Estimation (ISABLE) using a ceilometer and microwave radiometer, *Atmos. Meas. Tech.*, 2020, **13**, 6965–6987.

27 C. Flamant, J. Pelon, P. H. Flamant and P. Durand, Lidar determination of the entrainment zone thickness at the top of the unstable marine atmospheric boundary layer, *Bound.-Layer Meteorol.*, 1997, **83**, 247–284.

28 S. Emeis, K. Schäfer and C. Münkel, Surface-based remote sensing of the mixing-layer height – a review, *Meteorol. Z.*, 2008, **17**, 621–630.

29 Y. Morille, M. Haeffelin, P. Drobinski and J. Pelon, STRAT: an automated algorithm to retrieve the vertical structure of the atmosphere from single-channel lidar data, *J. Atmos. Oceanic Technol.*, 2007, **24**, 761–775.

30 D. Toledo, C. Córdoba-Jabonero and M. Gil-Ojeda, Cluster analysis: a new approach applied to lidar measurements for atmospheric boundary layer height estimation, *J. Atmos. Oceanic Technol.*, 2014, **31**, 422–436.

31 C. Fountoukis and A. Nenes, ISORROPIA II: a computationally efficient thermodynamic equilibrium model for K^+–Ca^{2+}–Mg^{2+}–NH_4^+–Na^+–SO_4^{2-}–NO_3^-–Cl^-–H_2O aerosols, *Atmos. Chem. Phys.*, 2007, **7**, 4639–4659.

32 S. Lim, J. Hwang, M. Lee, C. I. Czimczik, X. Xu and J. Savarino, Robust evidence of ^{14}C, ^{13}C, and ^{15}N analyses indicating fossil fuel sources for total carbon and ammonium in fine aerosols in Seoul megacity, *Environ. Sci. Technol.*, 2022, **56**, 6894–6904.

33 W. Tao, H. Su, G. Zheng, J. Wang, C. Wei, L. Liu, N. Ma, M. Li, Q. Zhang, U. Pöschl and Y. Cheng, Aerosol pH and chemical regimes of sulfate formation in aerosol water during winter haze in the North China Plain, *Atmos. Chem. Phys.*, 2020, **20**, 11729–11746.

34 M. Zhou, G. Zheng, H. Wang, L. Qiao, S. Zhu, D. Huang, J. An, S. Lou, S. Tao, Q. Wang, R. Yan, Y. Ma, C. Chen, Y. Cheng, H. Su and C. Huang, Long-term trends and drivers of aerosol pH in eastern China, *Atmos. Chem. Phys.*, 2022, **22**, 13833–13844.

35 S. Song, M. Gao, W. Xu, J. Shao, G. Shi, S. Wang, Y. Wang, Y. Sun and M. B. McElroy, Fine-particle pH for Beijing winter haze as inferred from different thermodynamic equilibrium models, *Atmos. Chem. Phys.*, 2018, **18**, 7423–7438.

36 Y. Cao, Z. Zhang, H. Xiao, Y. Xie, Y. Liang and H. Xiao, How aerosol pH responds to nitrate to sulfate ratio of fine-mode particulate, *Environ. Sci. Pollut. Res.*, 2020, **27**, 35031–35039.

37 H. Guo, R. J. Weber and A. Nenes, High levels of ammonia do not raise fine particle pH sufficiently to yield nitrogen oxide-dominated sulfate production, *Sci. Rep.*, 2017, **7**, 12109.

38 H. Guo, R. Otjes, P. Schlag, A. Kiendler-Scharr, A. Nenes and R. J. Weber, Effectiveness of ammonia reduction on control of fine particle nitrate, *Atmos. Chem. Phys.*, 2018, **18**, 12241–12256.

39 Y. Wang, Y. Chen, Z. Wu, D. Shang, Y. Bian, Z. Du, S. H. Schmitt, R. Su, G. I. Gkatzelis, P. Schlag, T. Hohaus, A. Voliotis, K. Lu, L. Zen, C. Zhao, M. R. Alfarra, G. McFiggans, A. Wiedensohler, A. Kiendler-Scharr, Y. Zhang and M. Hu, Mutual promotion between aerosol particle liquid water and particulate nitrate enhancement leads to severe nitrate-dominated particulate matter pollution and low visibility, *Atmos. Chem. Phys.*, 2020, **20**, 2161–2175.

40 S. Lim, X. Yang, M. Lee, G. Li, Y. Gao, X. Shang, K. Zhang, C. I. Czimczik, X. Xu, M.-S. Bae, K.-J. Moon and K. Jeon, Fossil-driven secondary inorganic $PM_{2.5}$ enhancement in the North China Plain: evidence from carbon and nitrogen isotopes, *Environ. Pollut.*, 2020, **266**, 115163.

41 A. Laskin, J. Laskin and S. A. Nizkorodov, Chemistry of atmospheric brown carbon, *Chem. Rev.*, 2015, **115**, 4335–4382.

42 M. Song, M. Lee, J. H. Kim, S. S. Yum, G. Lee and K.-R. Kim, New particle formation and growth in relation to vertical mixing and chemical species during ABC-EAREX2005, *Atmos. Res.*, 2010, **97**, 359–370.

43 T. D. Fairlie, D. J. Jacob, J. E. Dibb, B. Alexander, M. A. Avery, A. van Donkelaar and L. Zhang, Impact of mineral dust on nitrate, sulfate, and ozone in transpacific Asian pollution plumes, *Atmos. Chem. Phys.*, 2010, **10**, 3999–4012.

44 D. A. Peterson, E. J. Hyer, S.-O. Han, J. H. Crawford, R. J. Park, R. Holz, R. E. Kuehn, E. Eloranta, C. Knote, C. E. Jordan and B. L. Lefer, Meteorology influencing springtime air quality, pollution transport, and visibility in Korea, *Elem. Sci. Anthr.*, 2019, **7**, 57.

45 C.-H. Kim, H.-Y. Jo, Y.-J. Jo, H.-J. Lee, J.-M. Kim, N.-M. Lee, S.-Y. Jeong, S.-H. Baek, M.-J. Park, L.-S. Chang, J.-J. Lee and C.-K. Song, Synoptic meteorological conditions and contributing factors to air quality during the SIJAQ campaign, *Atmos. Environ.*, 2023, **309**, 119939.

46 M. Igawa, K. Kamijo, B. Nanzai and K. Matsumoto, Chemical composition of polluted mist droplets, *Atmos. Environ.*, 2017, **171**, 230–236.

47 J.-W. Yoo, S.-Y. Park, H.-Y. Jo, Y. Jeong, H.-J. Lee, C.-H. Kim and S.-H. Lee, Assessing the role of cold front passage and synoptic patterns on air pollution in the Korean Peninsula, *Environ. Pollut.*, 2024, **348**, 123803.

48 D. Zhao, J. Xin, C. Gong, J. Quan, Y. Wang, G. Tang, Y. Ma, L. Dai, X. Wu, G. Liu and Y. Ma, The impact threshold of the aerosol radiative forcing on the boundary layer structure in the pollution region, *Atmos. Chem. Phys.*, 2021, **21**, 5739–5753.

49 B. J. Turpin and H.-J. Lim, Species contributions to $PM_{2.5}$ mass concentrations: revisiting common assumptions for estimating organic mass, *Aerosol Sci. Technol.*, 2001, **35**, 602–610.

50 A. W. Stelson and J. H. Seinfeld, Relative humidity and temperature dependence of the ammonium nitrate dissociation constant, *Atmos. Environ.*, 1982, **16**, 983–992.

51 M. Z. Markovic, K. L. Hayden, J. G. Murphy, P. A. Makar, R. A. Ellis, R. Y.-W. Chang, J. G. Slowik, C. Mihele and J. Brook, The effect of meteorological and chemical factors on the agreement between observations and predictions of fine aerosol composition in southwestern Ontario during BAQS-Met, *Atmos. Chem. Phys.*, 2011, **11**, 3195–3210.

52 A. Ianniello, F. Spataro, G. Esposito, I. Allegrini, M. Hu and T. Zhu, Chemical characteristics of inorganic ammonium salts in $PM_{2.5}$ in the atmosphere of Beijing (China), *Atmos. Chem. Phys.*, 2011, **11**, 10803–10822.

53 A. C. Jones, A. Hill, S. Remy, N. L. Abraham, M. Dalvi, C. Hardacre, A. J. Hewitt, B. Johnson, J. P. Mulcahy and S. T. Turnock, Exploring the sensitivity of atmospheric nitrate concentrations to nitric acid uptake rate using the Met Office's Unified Model, *Atmos. Chem. Phys.*, 2021, **21**, 15901–15927.

54 S. Lim, M. Lee and H.-J. Yoo, Size distributions, mixing state, and morphology of refractory black carbon in an urban atmosphere of Northeast Asia during summer, *Sci. Total Environ.*, 2023, **856**, 158436.

55 X. Wang, W. Wang, L. Yang, X. Gao, W. Nie, Y. Yu, P. Xu, Y. Zhou and Z. Wang, The secondary formation of inorganic aerosols in the droplet mode through heterogeneous aqueous reactions under haze conditions, *Atmos. Environ.*, 2012, **63**, 68–76.

56 S. Lim, M. Lee, P. Laj, S.-W. Kim, K.-H. Ahn, J. Gil, X. Shang, M. Zanatta and K.-S. Kang, Regional characteristics of fine aerosol mass increase elucidated from long-term observations and KORUS-AQ campaign at a Northeast Asian background site, *Elem. Sci. Anthr.*, 2022, **10**, 00020.

57 C. E. Kolb and D. R. Worsnop, Chemistry and composition of atmospheric aerosol particles, *Annu. Rev. Phys. Chem.*, 2012, **63**, 471–491.

58 S. Zhang, X. Xu, Y. Lei, D. Li, Y. Wang, S. Liu, C. Wu, S. Ge and G. Wang, Smog chamber simulation on heterogeneous reaction of O_3 and NO_2 on black carbon under various relative humidity conditions, *Sci. Total Environ.*, 2022, **823**, 153649.

59 C. Zhang, S. Hai, Y. Gao, Y. Wang, S. Zhang, L. Sheng, B. Zhao, S. Wang, J. Jiang, X. Huang, X. Shen, J. Sun, A. Lupascu, M. Shrivastava, J. D. Fast, W. Cheng, X. Guo, M. Chu, N. Ma, J. Hong, Q. Wang, X. Yao and H. Gao, Substantially positive contributions of new particle formation to cloud condensation nuclei under low supersaturation in China based on numerical model improvements, *Atmos. Chem. Phys.*, 2023, **23**, 10713–10730.

60 C. Yun, J. Kim, J. Lee, J. Lee, J. Gil, M. Lee and G. Lee, Nocturnal downward transport of NO_3 radical from the residual layer to a surface site by the mountain breeze in Seoul, South Korea, *Atmos. Environ.*, 2024, **321**, 120345.

61 S. S. Brown, H. An, M. Lee, J.-H. Park, S.-D. Lee, D. L. Fibiger, E. E. McDuffie, W. P. Dubé, N. L. Wagner and K.-E. Min, Cavity enhanced spectroscopy for measurement of nitrogen oxides in the Anthropocene: results from the Seoul tower during MAPS 2015, *Faraday Discuss.*, 2017, **200**, 529–557.

62 T. Su, Z. Li, N. R. Henao, Q. Luan and F. Yu, Constraining effects of aerosol-cloud interaction by accounting for coupling between cloud and land surface, *Sci. Adv.*, 2024, **10**, eadl5044.

